*Korean J. Chem. Eng.*, 34(9), 2366-2373 (2017)
DOI: 10.1007/s11814-017-0159-1

pISSN: 0256-1115
eISSN: 1975-7220

# CFD analysis for the geometry effect of disc-type membrane module on separation performance

**Geunjeong Lee*, Kyung-Ran Hwang**, Jong-Soo Park***, and Myung-June Park*,****,†**

*Department of Energy Systems Research, Ajou University, Suwon 16499, Korea
**Clean Fuel Department, Korea Institute of Energy Research, Daejeon 34129, Korea
***Energy Materials Center, Korea Institute of Energy Research, Daejeon 34129, Korea
****Department of Chemical Engineering, Ajou University, Suwon 16499, Korea

(*Received 6 March 2017 • accepted 3 June 2017*)

**Abstract**−A disc-type Pd-Au membrane module was considered, and a computational fluid dynamics (CFD) model was developed to describe the actual flow dynamics and the distribution of $H_2$ flux over the membrane. When the membrane size was increased to develop a module with a large separation capacity, the feed flow rate per unit membrane area decreased, indicating loss of utilization of the membrane area. To increase the utilization, the sizes of the feed inlet tube and retentate tube were varied (cases 1 and 2, respectively). The CFD simulation showed that the feed flow rates per unit membrane area increased by *ca.* 8% and 10%, respectively, whereas a change in the geometry from circular to a rectangle with rounded edges (case 3) resulted in an increase of approximately 19%. A change in the ratio of the edges (case 4) had a slight influence on the separation performance. The distribution of $H_2$ flux where the geometries in cases 1-3 were combined clearly revealed that most of the membrane area was used to permeate $H_2$; as a result, the number of membranes decreased by approximately 88% upon increasing their size, while the total membrane area remained the same. This indicated improved utilization of the membrane. The proposed approach is expected to be useful for acquiring valuable information on the design of a membrane module with a large separation capacity.

Keywords: Disc-type Membrane, Computational Fluid Dynamics Model, Membrane Geometry, Hydrogen Flux, Scale-up

## INTRODUCTION

Precombustion, which is one of the $CO_2$ capture processes, includes the production of synthesis gas (CO and $H_2$), removal of $CO_2$, and combustion of $H_2$. Synthesis gas is produced from a variety of feedstock materials such as natural gas, naphtha, heavy oils, and coal by the reforming, partial oxidation, and water-gas shift reactions [1]. The $H_2$ yield is increased via conversion of CO to $CO_2$ and $H_2$ through the water-gas shift reaction; this is followed by the $CO_2$ removal process, for which either $H_2$- or $CO_2$-selective membranes can be used [2]. Several types of $CO_2$-selective membranes have been reported, such as polypropylene [3], polytetrafluoroethylene [4], and polybenzimidazole/polyvinylidene [5] membranes; examples of $H_2$-selective membranes include Pd-based membranes and hybrid organo-silica membranes.

For membranes to be useful for $CO_2$ capture, they must have high permeability, high selectivity, and high physical and chemical resistance, in addition to being cost effective [6,7]. Gas separation properties such as permeability, separation factor, and permeance are strongly dependent on membrane material, structure, thickness, and configuration (e.g., a flat, hollow fiber), as well as on the membrane module and system design [8]. The membrane thickness is crucial for improving the permeation flux [9] and mitigating the effects of contamination [10]. However, despite the fact that extremely high fluxes can be achieved with thin membranes, the external mass transfer resistance can become significant, especially on the low-partial-pressure side of the membrane and when a porous support is present [9].

The structure of a membrane module has been altered to enhance the mass transfer performance. Liu et al. [11] proposed a coiled hollow fiber membrane module and showed that its mass transfer coefficient was higher than that of a straight module, up to 3.5 times higher under the condition of an identical membrane area, owing to the secondary flow in the coiled tube and the enhanced turbulence on the shell side. Jaffrin reported enhancement of the membrane shear rate necessary to maintain dynamic filtration through the use of a rotating disk, which also increased both the permeate flux and the membrane selectivity [12]. In other works, a plate-type Pd-Au membrane was prepared over a porous metal support by sputtering and sintering procedures [13,14], and it was demonstrated that the module configuration could minimize the polarization effects of the gas mixture concentration.

Several research works have been conducted with a focus on applying the modeling approach to understand the governing behavior of membrane modules and to improve their performance. Boon et al. [15] applied a modeling approach to quantify the effects of inhibitors (such as CO, $CO_2$, and steam) that are adsorbed at the Pd-membrane surface for the separation of $H_2$. Chen et al.

---

†To whom correspondence should be addressed.
E-mail: mjpark@ajou.ac.kr

developed a two-dimensional numerical method to simulate the phenomenon of concentration polarization for hydrogen permeation in a Pd-based membrane tube [16]. Takaba and Nakao [17] modeled actual fluid dynamics in complex geometries by using the computational fluid dynamics (CFD) method and considered the concentration polarization effect as a function of the feed rate, selectivity, operating pressure, mass transfer coefficient, and module geometry. Grahn and Hedlund [18] developed a mathematical model for high-flux tubular silicalite-1 membranes and showed that the membrane selectivity can be improved by reducing the flow-through defects and by preparing supports with lower flow resistance. Ramírez-Santos et al. reviewed the modeling development of inorganic microporous membranes for $H_2$ and $CO_2$ separation [19]. Modeling can also be used to investigate the feasibility of selective layer membranes in industrial hydrogen production applications [19-21]. Pd-based membranes have been benchmarked for precombustion $CO_2$ capture by achieving the permeation of $H_2$ in industrially relevant conditions [22]. Recently, CFD was applied to evaluate the effects of a micro-channel turbulence promoter with micro-pores on the turbulent flow in a flat-sheet membrane channel [23] and to investigate the effects of module geometry on the separation performance [24].

In our previous work [25], we developed a plate-type Pd-Au membrane module for application to a precombustion $CO_2$ capture process. This module was scaled up for industrial application by stacking unit modules, as is done in a microreaction system; therefore, a very small membrane leads to unbalanced geometry of the entire module, with a very large height-to-width ratio, or to the requirement of a large number of entire modules, thereby increasing capital cost. However, an increase in the size (diameter) of the unit membrane from 2 in to 3.5 in was observed to decrease the feed flow rate per unit membrane area for a 90% $CO_2$ fraction in the retentate; thus, the utilization of the separation area was partially lost. In the present study, with the aim of increasing the efficiency of large membranes to the level of that of small ones, the CFD modeling approach was therefore employed along with detailed fluid dynamics for evaluating the effects of membrane geometry on the separation performance under the assumption of its application to the actual feed gas of the separation module in the precombustion $CO_2$ capture process [26].

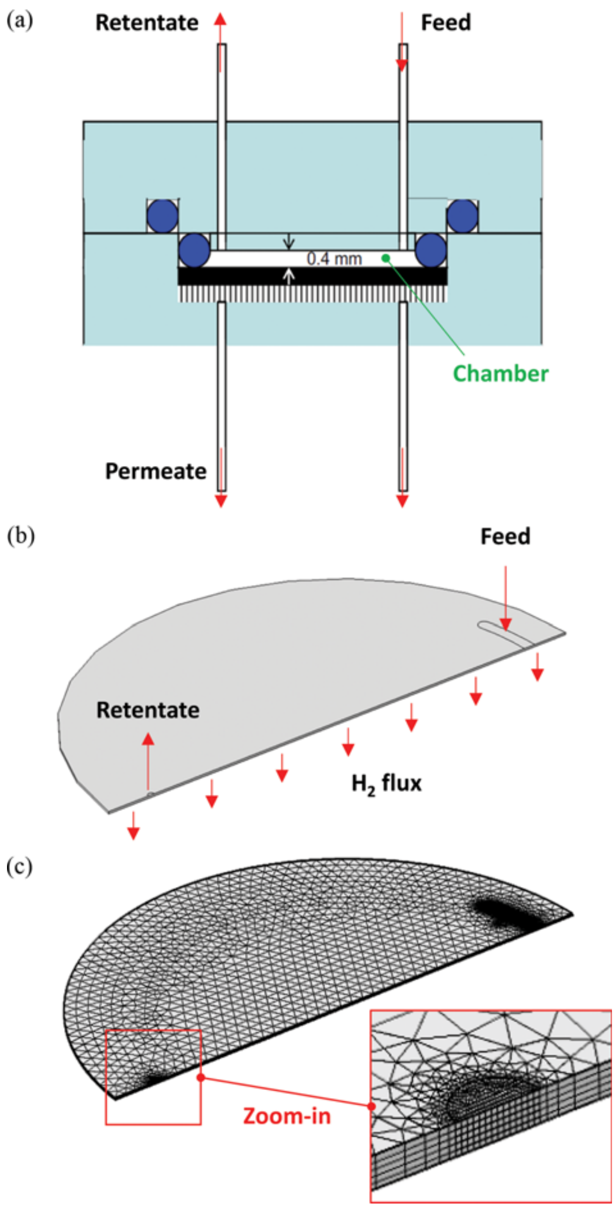

**Fig. 1. (a) Schematic diagram of disc-type $CO_2$ capture module using Pd-based membrane, (b) structure of chamber realized in COMSOL Multiphysics (COMSOL Inc.) software, and (c) distribution of meshes specified for calculations.**

## MATHEMATICAL MODELING

The diameter of the membrane considered in the present study was 3.5 in, and the diameter and height of the chamber were 81.4 mm and 0.4 mm, respectively. Feed enters from the feed inlet tube, and $H_2$ permeates through the membrane while the remaining gas exits through the retentate tube. The scheme of the membrane module is shown in Fig. 1; to reduce the computational burden, only one-half of the module was simulated under the assumption of symmetry.

Simulation was performed using the COMSOL Multiphysics® software, in which the *PARDISO* solver was incorporated. Two built-in modules in the software package were used here: the laminar flow module and the transport of concentrated species module were, respectively, used to consider total momentum and mass balances, and component mass balances in the chamber. Detailed governing equations and boundary conditions are listed in Table 1. Galerkin's method [27] was employed for the calculation, and 63,130 free trigonal grids were defined (Fig. 1(c)); a large number of grids were assigned for the feed inlet and retentate tubes to satisfy the overall mass balances.

$H_2$ flux in the membrane was calculated by using the following equation:

$$N_{H_2}=Q'(P^{n}_{chamber}-P^{n}_{permeate}) \quad (1)$$

where $N_{H_2}$ and $Q'$ denote $H_2$ flux [mol/(m$^2$·s)] and permeance [mol/(m$^2$·s·kPa$^n$)], respectively, and $P_j$ denotes partial pressure. The superscript n represents the pressure exponent, which is known

**Table 1. Governing equations and boundary conditions considered in the present study**

| Name | Equations and boundary conditions |
|---|---|
| Laminar flow (momentum balance) | $\nabla\cdot(\rho\mathbf{u})=0$<br>$\rho\mathbf{u}\cdot\nabla\mathbf{u}=-\nabla \mathrm{p}+\nabla\cdot\left(\mu(\nabla\mathbf{u}+(\nabla\mathbf{u})^T)-\frac{2}{3}\mu(\nabla\cdot \mathrm{u})\mathbf{I}\right)+\mathbf{F}$<br>B.C.'s<br>$\mathbf{u}=-\mathrm{U}_0\mathbf{n}$ (inlet)<br>$\mathbf{n}^T\left[-\mathrm{p}\mathbf{I}+\mu(\nabla\mathbf{u}+(\nabla\mathbf{u})^T)-\frac{2}{3}\mu(\nabla\cdot\mathbf{u})\mathbf{I}\right]\mathbf{n}=-\hat{\mathrm{p}}_0$ (outlet)<br>$\mathbf{u}=0$ (wall) |
| Transport of concentrated species (mass balance) | $\nabla\cdot(\rho\omega_i\mathbf{u})=-\nabla\cdot\mathbf{j}_i+\mathrm{R}_i$<br>where<br>$\mathbf{j}_i=-\left(\rho\mathrm{D}_i^m\nabla\omega_i+\rho\omega_i\mathrm{D}_i^m\frac{\nabla\mathrm{M}}{\mathrm{M}}+\mathrm{D}_i^T\frac{\nabla\mathrm{T}}{\mathrm{T}}\right)$<br>$\mathrm{D}_i^m=\frac{1-\omega_i}{\Sigma_{k\neq1}^N\frac{\mathrm{x}_k}{\mathrm{D}_{ik}}},\ \mathrm{D}_{ik}=\frac{0.00143\mathrm{T}^{1.75}}{\mathrm{P}(\mathrm{M}_{AB}^{1/2})[(\Sigma\mathrm{v}_A)^{1/3}+(\Sigma\mathrm{v}_B)^{1/3}]^2}$<br>B.C.'s<br>$\omega_i=\omega_{0,i}=\mathrm{x}_{0,i}\mathrm{M}_i/\mathrm{M}_n$ (inflow)<br>$-\mathbf{n}\cdot\rho\mathrm{D}_i^m\nabla\omega_i=0$ (outflow) |

to be dependent on the surface reaction and on other factors such as defects, impurities, and support resistance that were involved in the hydrogen permeation behavior [28-30]. The values of n and Q′ were determined to be 0.752 and $1.01\times10^{-3}$, respectively, by fitting of experimental data under different pressures (Fig. 2(a)). The regression line was determined such that its intercept passed through the origin. As shown in Fig. 2(b), the values determined by the simulation were in good agreement with the experimental data. Also, because the permeance is a unique property determined by the characteristics of the membrane only and independent from the operating conditions except temperature, the parameter was considered as a constant.

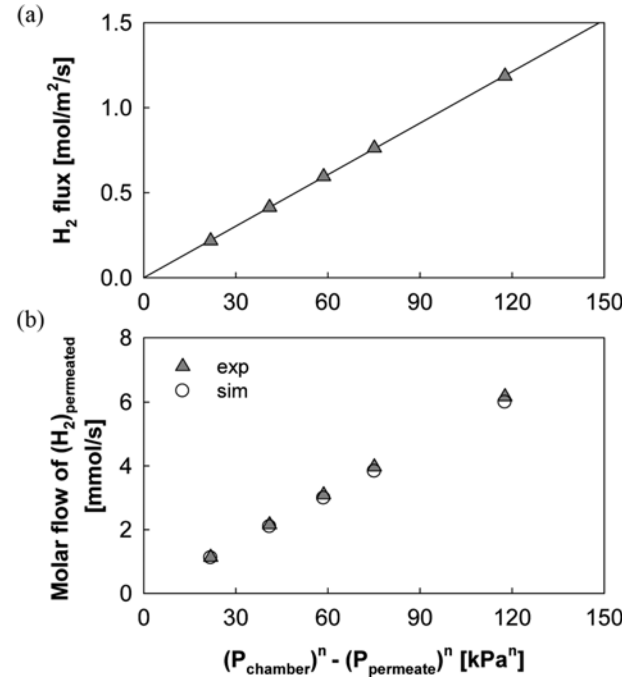

**Fig. 2. (a) Determination of permeance (Q′) and pressure exponent (n); the solid line represents the regression results, $y=1.01\times10^{-3}x$ with n=0.752 ($R^2=0.9999$). (b) Comparison of molar flow rate of permeated $H_2$ between experimental data and simulated results (mean of absolute relative residuals=2.9%, relative standard deviation of individual errors=0.63%).**

## RESULTS AND DISCUSSION

The CFD model was applied to a gas mixture considered in our previous work [26], where $H_2O$ in the effluent of the water-gas shift reactor was removed using a flash separator and small-sized membranes (2 in) were then used to separate $H_2$ from the mixture. The composition of the gas mixture was $CO_2/H_2/CO/N_2/H_2O$=40.0%/57.9%/0.11%/1.16%/0.83% with a total flow rate of 2.5 $Nm^3$/min (111.5 gmol/min) corresponding to the flue gas flow rate of 100 $Nm^3$/h, and the pressure and temperature were maintained at 30 bar and 400 °C, respectively. Note that a Pd-Au composite membrane deposited on a porous nickel support shows a high $H_2$ permeation flux even in the case of the $CO_2/H_2$ mixture; this is attributed to the unique preparation method of the disc-shaped, thin Pd-based membrane [31] and the module configuration, which minimized the polarization effect of the gas mixture concentration [25]. So, the flux is dependent on the partial pressure of hydrogen even in the existence of the other gases in the mixture, and this feature was experimentally corroborated in our previous work [32]. Therefore, Eq. (1), in which $H_2$ flux is expressed as a function of the partial pressure of $H_2$, was used without modification.

Fig. 3 shows the simulation results for 3.5-in membranes at various feed flow rates. Since the threshold value of the $CO_2$ fraction

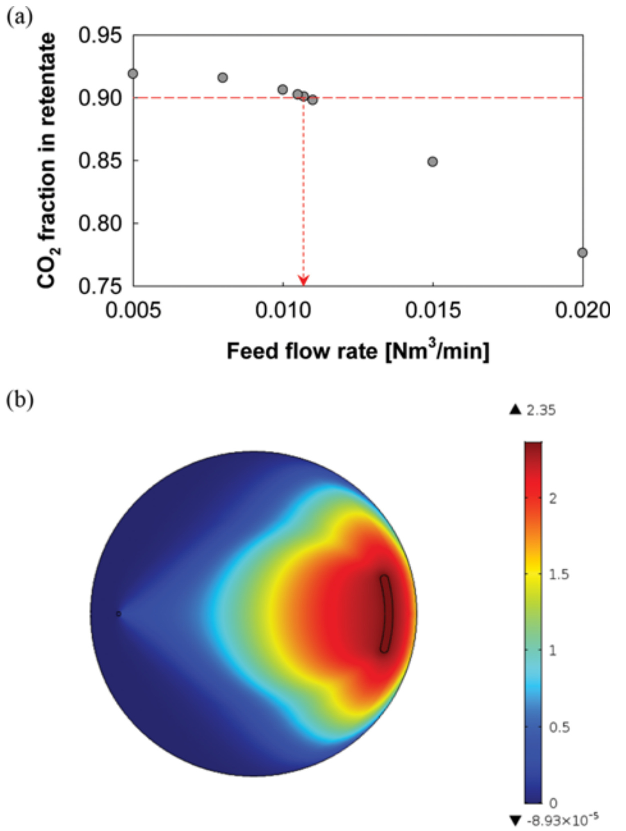

**Fig. 3. (a) $CO_2$ fraction in retentate ($x_{CO_2}$) as a function of feed flow rate; the flow rate (F) for the threshold fraction is $10.7\times10^{-3}$ $Nm^3/min$, and the corresponding flow rate per unit membrane area ($F^S$=F/S) is 2.06 $Nm^3/(m^2\cdot min)$. (b) Distribution of $H_2$ flux in membrane ($P_{chamber}$=30 bar, $P_{permeate}$=1 bar) at $x_{CO_2}$= 0.90.**

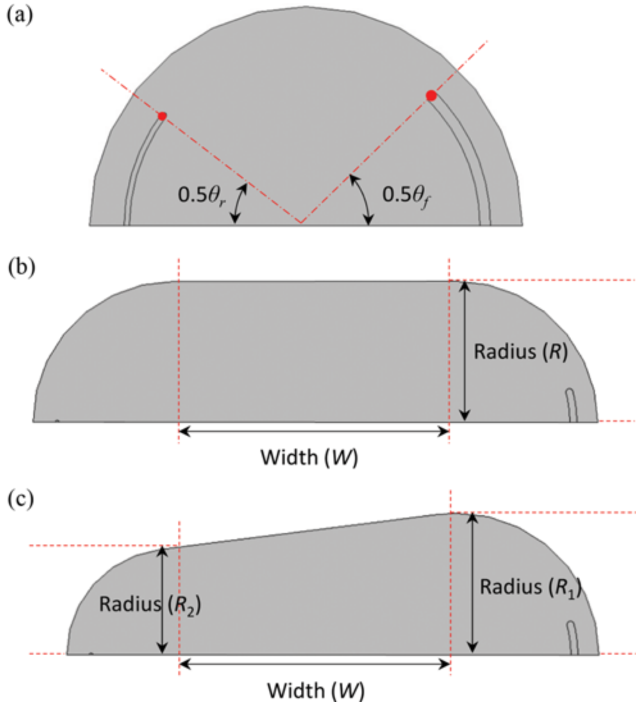

**Fig. 4. Definitions of variables considered in the present study. (a) Cases 1 and 2: change in angles of feed inlet tube ($\theta_f$) and retentate tube ($\theta_r$), respectively; (b) Case 3: change in width (W) under fixed radius (R); and (c) Case 4: change in $R_2$ under fixed $R_1$.**

permissible in the retentate was specified to be 0.90, the corresponding feed flow rate was determined to be $1.07\times10^{-2}$ $Nm^3/min$, and the feed flow rate per unit membrane area ($F^S$) was calculated to be 2.06 $Nm^3/(m^2\cdot min)$. The total surface area required to handle the effluent flow rate of 2.5 $Nm^3/min$ was calculated to be 1.22 $m^2$, whereas the total surface area required for 2-in membranes was 0.971 $m^2$ ($F^S$=2.57 $Nm^3/(m^2\cdot min)$). This result indicates that loss of separation efficiency occurred when the size of the unit membrane was increased from 2 in to 3.5 in; this was despite the fact that the total number of membranes decreased from 585 (2 in) to 234 (3.5 in), which resulted in a decrease in the height of the entire module that was fabricated by stacking up membranes.

To evaluate the effects of membrane geometry on the separation performance, the size of the feed inlet tube was increased (hereafter referred to as case 1) by changing its angle ($\theta_f$) from the center (*cf.* Fig. 4(a)); the results are shown in Fig. 5. The value of the feed flow rate per unit membrane area ($F^S$) for $x_{CO_2}$=0.90 with $\theta_f$=30° (Fig. 3) was taken as the reference case ($F^S_{ref}$=2.06 $Nm^3/(m^2\cdot min)$, indicated by the red star in Fig. 5(a)). It was seen that $x_{CO_2}$ decreased with increasing feed flow rate, owing to the reduced residence time in the chamber; however, an increase in $\theta_f$ led to an increase in $x_{CO_2}$ owing to the increased $H_2$ flux around the feed inlet tube. This behavior was reflected in the distribution of $H_2$ flux in the membrane (Fig. 5(c)), where most of the right-half of the plane was used for the permeation of $H_2$, although the utilization of the left-half of the plane, especially around the center, was slightly lower than that in the reference case. As a result, when the feed inlet tube was widened to $\theta_f$=90°, the feed flow rate per unit membrane area ($F^S$) increased by approximately 8% and the corresponding value of the total membrane area ($S_{total}$) for the entire module decreased.

In case 2, the retentate tube was widened; Fig. 6 shows the results for this case. An increase in the angle of the retentate tube caused an increase in $x_{CO_2}$; a further increase in the angle led to an increment in the degree of increase in $x_{CO_2}$. As shown in Fig. 5(c) ($\theta_r$=90°), the pattern of the $H_2$ flux distribution was similar to that in the reference case, whereas the area of high flux (indicated in red, yellow, green, and light blue) was wider than that in the reference case. In addition, the upper and lower parts of the left-half of the plane changed from dark blue to blue in color (the scale of the colormap was specified to be the same for all the cases), indicating that the unused parts were additionally utilized in this case. The effects of the size of the retentate tube were larger than those of the feed inlet tube, and thus, a 10% increase in the feed flow rate per unit membrane area ($F^S$) and a decrease in the total membrane area ($S_{total}$) could be achieved by increasing the angle ($\theta_r$) to 90°.

As observed in cases 1 and 2, the circular geometry of the membrane provided relatively low fluxes in the upper and lower parts. This result is attributed to the fact that these parts correspond to the relatively long path of the gas streams from the feed inlet tube

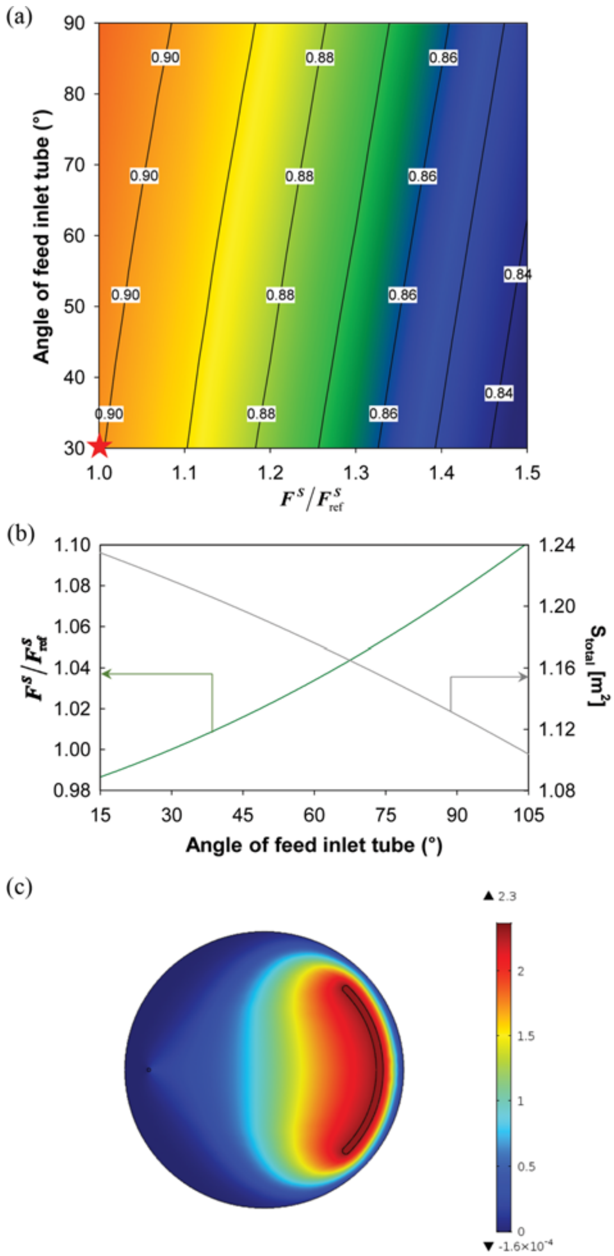

**Fig. 5. (a) Contour plot of $x_{CO_2}$ as a function of feed inlet tube angle ($\theta_f$) and scaled values of feed flow rate per unit membrane area ($F^S/F^S_{ref}$), where $F^S_{ref}$=2.06 Nm$^3$/(m$^2$·min). The red star represents the reference case shown in Fig. 3. (b) Scaled values of feed flow rate per unit membrane area for $x_{CO_2}$=0.90 (left ordinate) and total membrane area ($S_{total}$) required to handle flue gas flow rate of 150 Nm$^3$/h (right ordinate) [26]. (c) Distribution of $H_2$ flux in membrane ($P_{chamber}$=30 bar, $P_{permeate}$=1 bar) with $\theta_f$=90° and $\theta_r$=0°.**

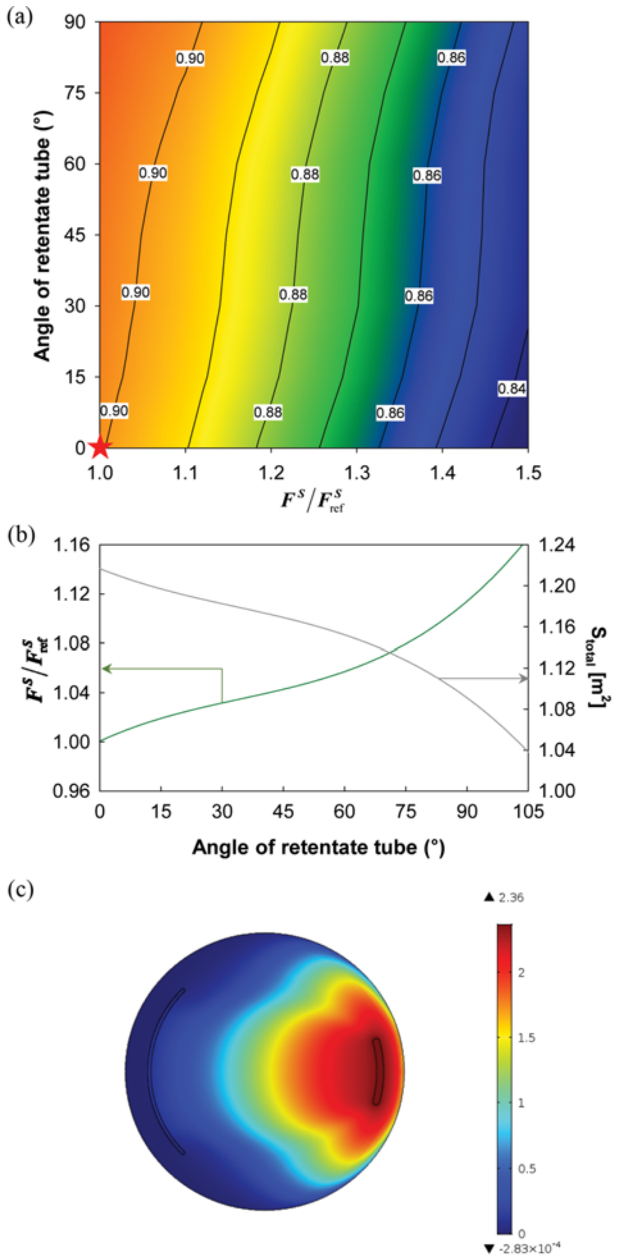

**Fig. 6. (a) Contour plot of $x_{CO_2}$ as a function of retentate tube angle ($\theta_r$) and scaled values of feed flow rate per unit membrane area ($F^S/F^S_{ref}$), where $F^S_{ref}$=2.06 Nm$^3$/(m$^2$·min). (b) Scaled values of feed flow rate per unit membrane area for $x_{CO_2}$=0.90 (left ordinate) and total membrane area ($S_{total}$) required to handle flue gas flow rate of 150 Nm$^3$/h (right ordinate) [26]. (c) Distribution of $H_2$ flux in membrane ($P_{chamber}$=30 bar, $P_{permeate}$=1 bar) with $\theta_f$=30° and $\theta_r$=90°.**

to the retentate tube. To eliminate such detour paths, the geometry was changed to a rectangle with rounded edges (*cf.* Fig. 4(b); referred to as case 3). The value of $x_{CO_2}$ increased substantially with an increase in W/R, and it saturated when the ratio became higher than about 2.5 (Fig. 7(a)). The value of $F^S/F^S_{ref}$ for W/R=2.5 was about 1.24, corresponding to a 19% reduction in $S_{total}$ in comparison to the reference case (Fig. 7(b)). As shown in Fig. 7(c), the portion of the blue-colored area decreased; thus, the utilization of the membrane area improved significantly. Direct flow of the gas from the feed inlet tube to the retentate tube could be distinguished from indirect flow with greater clarity (i.e., rightward flows from the feed inlet tube turned in the upward/downward direction when they reached the wall and then turned leftward to the retentate tube). As a result, low-flux regions came into existence (*cf.* the white-edged

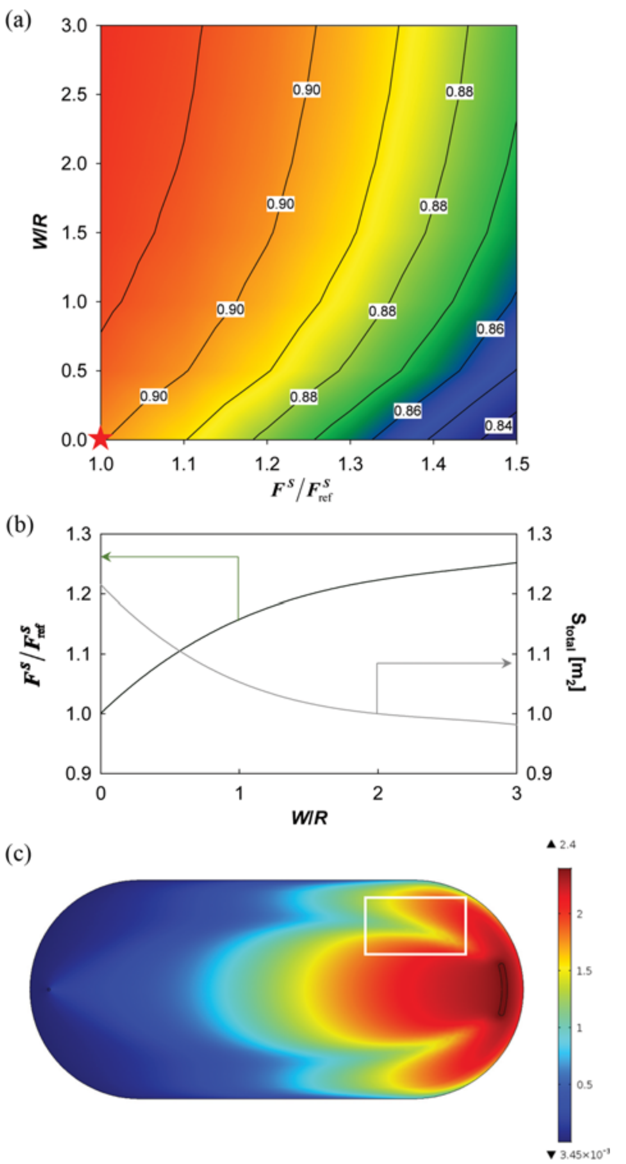

**Fig. 7.** (a) Contour plot of $x_{CO_2}$ as a function of width/radius (W/R) and scaled values of feed flow rate per unit membrane area ($F^S/F^S_{ref}$), where $F^S_{ref}$=2.06 Nm$^3$/(m$^2$min). (b) Scaled values of feed flow rate per unit membrane area for $x_{CO_2}$=0.90 (left ordinate) and total membrane area ($S_{total}$) required to handle flue gas flow rate of 150 Nm$^3$/h (right ordinate) [26]. (c) Distribution of $H_2$ flux in membrane ($P_{chamber}$=30 bar, $P_{permeate}$ =1 bar) with W/R=2.5, $\theta_f$=30°, and $\theta_r$=0°.

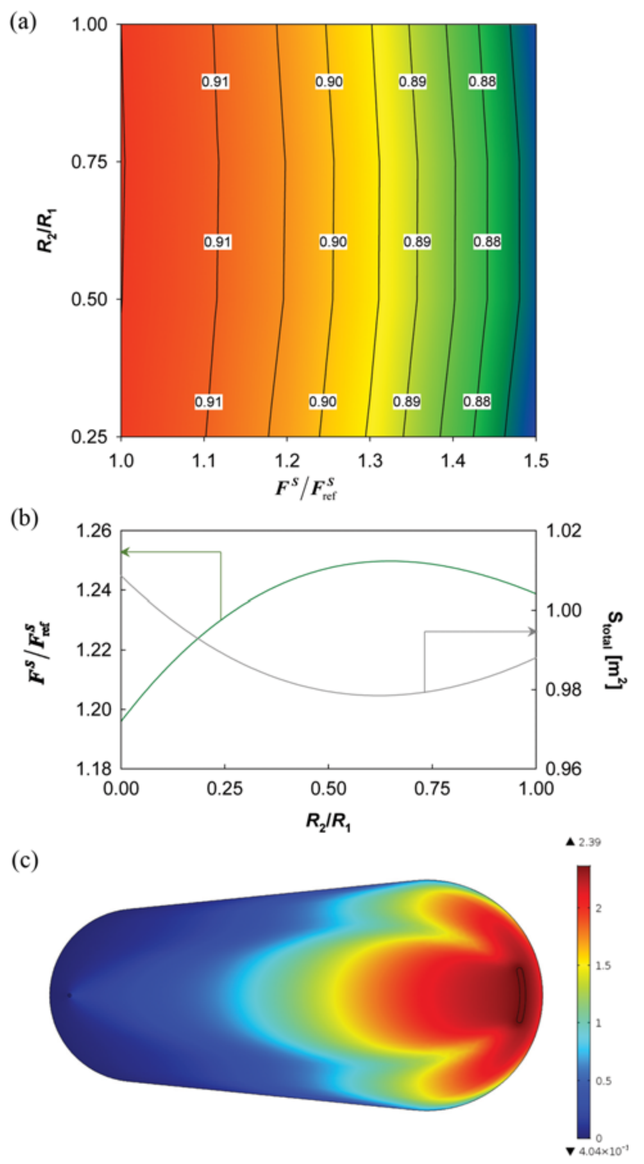

**Fig. 8.** (a) Contour plot of $x_{CO_2}$ as a function of $R_2/R_1$ and scaled values of feed flow rate per unit membrane area ($F^S/F^S_{ref}$), where $F^S_{ref}$=2.06 Nm$^3$/(m$^2$min). (b) Scaled values of feed flow rate per unit membrane area for $x_{CO_2}$=0.90 (left ordinate) and total membrane area ($S_{total}$) required to handle flue gas flow rate of 150 Nm$^3$/h (right ordinate) [26]. (c) Distribution of $H_2$ flux in membrane ($P_{chamber}$=30 bar, $P_{permeate}$=1 bar) with W/R =2.5, $\theta_f$=30°, $\theta_r$=0°, and $R_2/R_1$=0.75.

box in Fig. 7(c)).

Since an unused area in the upper and lower parts of the left-half of the plane was observed even in case 3, the geometry was changed further: the left-side edge was narrowed while W/R was fixed at 2.5 (referred to as case 4). As shown in Fig. 8, when the edge was narrowed, $x_{CO_2}$ increased slightly because of elimination of the unused area. However, a further narrowing of the edge led to a reduction in the area of the right-half of the plane, resulting in a decrease in $x_{CO_2}$. Overall, the effects of the change in $R_2/R_1$ were insignificant in comparison to the effects of geometry changes in the other cases. Note that, in the laminar flow module, the pressure was assumed to be constant over the entire chamber under the assumption that the pressure drop was negligible. The change of membrane geometry may have led to different profile of pressure drop along the chamber and the corresponding profile of local velocity. Although this impact might become significant when the width gets much bigger than the radius, weak dependence of pressure drop was assumed in the present study with W/R lower than 3.

Fig. 9 summarizes the results of all cases, where it can be seen that the total membrane area in the reference case (1.217 m$^2$) was 25.3% higher than that in the case of the 2-in membranes (0.9711

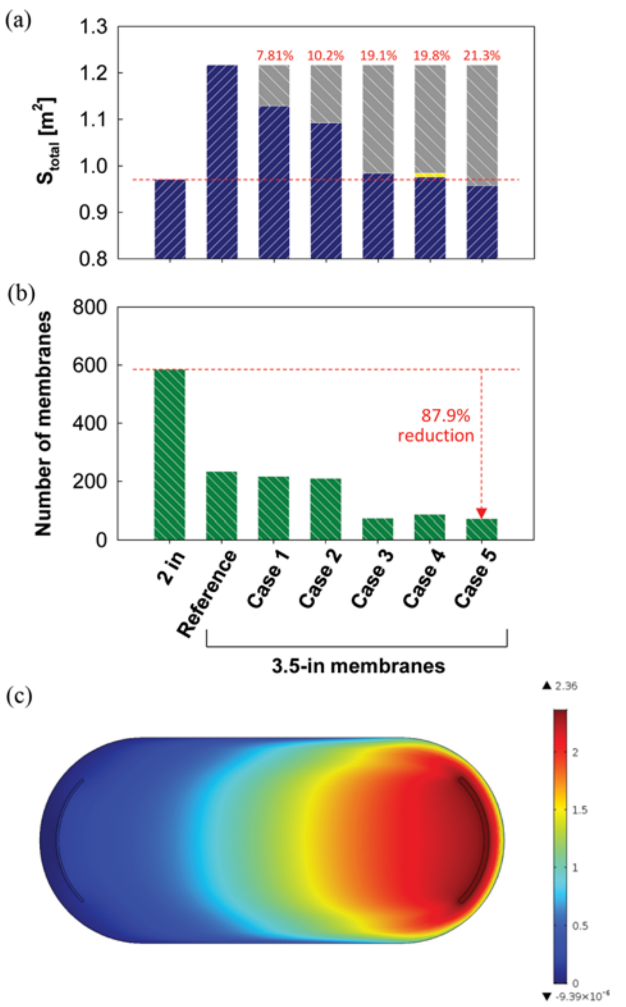

**Fig. 9. Comparisons of (a) total membrane area ($S_{total}$), where the gray shaded areas and red numerals represent the parts and relative percentage, respectively, reduced from the reference case (Case 5 is the combination of Cases 1-3) and (b) number of membranes between the cases considered in the present study. (c) Distribution of $H_2$ flux in membrane ($P_{chamber}$= 30 bar, $P_{permeate}$=1 bar) with W/R=2.5 and $\theta_f=\theta_r=90^o$.**

m$^2$). Case 3, in which the geometry was changed to the rectangle with rounded edges, showed the largest reduction in the total membrane area (19.1%), which made this total membrane area almost identical to that in the case of the 2-in membranes. In case 4, $R_2/R_1$ was varied according to case 3 (W/R=2.5), and thus, the net effects of case 4 were only 0.7% point (yellow bar in Fig. 9(a)). Therefore, a simulation was performed by combining the geometries in cases 1-3 (referred to as case 5), and consequently, the total membrane area reduced further to 0.9573 m$^2$; this is marginally lower than the total membrane area in the case of the 2-in membranes, and it corresponds to a 21.3% reduction from the reference case. The resulting number of membranes for the entire module was determined to be 71, which corresponds to a reduction of about 88% from the case with 2-in membranes. Thus, the height of the module in case 5 decreased to one-tenth of that in the module with 2-in membranes. As shown in Fig. 9(c), the widened tube combined the direct and indirect flows to make the velocity distribution similar to a hyperbolic profile and eliminated most of the unused parts (dark blue), except those on the left-hand side of the retentate tube, for maximal utilization of the membranes.

## CONCLUSIONS

Various velocity distributions exist in a disc-type membrane module because of the presence of a variety of trajectories from the feed inlet tube to the retentate tube. Therefore, the geometry of the membrane module, which determines the velocity profiles of gas streams, significantly influences the local partial pressures of $H_2$ over the membrane surface. Since the CFD model developed in the present study considers the actual flow dynamics in the chamber of the module, the distribution of $H_2$ flux over the membrane surface could be satisfactorily described, and the developed model was used to evaluate the effects of the membrane geometry on the utilization of the membrane area. It was observed that a change in the geometry from circular to a rectangle with rounded edges corresponded to the elimination of rather long paths from the inlet to the outlet of the chamber, i.e., the unused parts of the membrane, and the separation efficiency could be maintained even after increasing the membrane size. This outcome could prevent a large increase in the height of the entire module, which is composed of many membrane chambers for achieving a large separation capacity. In conclusion, the proposed CFD-modeling-based approach can be used to design effective membrane modules.

## ACKNOWLEDGEMENTS

This research was supported by the C1 Gas Refinery Program through the National Research Foundation of Korea (NRF) funded by the Ministry of Science, ICT & Future Planning (NRF-2016M3D3A1A01916841), and by the Human Resources Development of the KETEP grant funded by the Ministry of Trade, Industry & Energy of the Korean Government (No. 20154010200820).

## NOMENCLATURE

$D_{ik}$ : binary diffusion coefficient between species i and k [m$^2$/s]
F : feed flow rate [Nm$^3$/min]
**F** : volume force vector [N/m$^3$]
$F^S$ : feed flow rate per unit area of membrane [Nm$^3$/(m$^2$·min)]
**j** : permeate flux [kg/(m$^2$·s)]
$N_{H_2}$ : $H_2$ flux at boundary between chamber and membrane [mol/(m$^2$·s)]
n : pressure exponent
**n** : normal vector
M : molecular weight, kg/mol
$M_{AB}$ : average molecular weight of species A and B [kg/mol]
$M_n$ : average molecular weight of all components in fluid
$P_{chamber}$ : partial pressure on chamber side of membrane [kPa]
$P_{permeate}$ : partial pressure on permeate side of membrane [kPa]
p : pressure of fluid [Pa]
$\hat{p}_0$ : outlet pressure [Pa]
Q′ : permeance [mol/(m$^2$·s·kPa$^n$)]

R : radius of membrane [mm]
$R_i$ : production or consumption rate [kg/(m$^3$·s)]
S : surface area of unit membrane [m$^2$]
$S_{total}$ : total surface area [m$^2$]
T : chamber temperature [K]
$U_0$ : normal inflow speed [m/s]
**u** : velocity of fluid [m/s]
v : atomic diffusion volumes
W : width of membrane, mm
$x_0$ : mole fraction of inflow
$x_{CO_2}$ : $CO_2$ mole fraction in retentate

**Greek Letters**
$\theta$ : angle
$\mu$ : viscosity of fluid
$\rho$ : density of fluid
$\omega$ : mass fraction

**Subscripts**
f : feed inlet tube
r : retentate tube
ref : reference case

## REFERENCES

1. R. Steeneveldt, B. Berger and T. A. Torp, *Chem. Eng. Res. Des.*, **84**, 739 (2006).
2. C. A. Scholes, K. H. Smith, S. E. Kentish and G. W. Stevens, *Int. J. Greenhouse Gas Control*, **4**, 739 (2010).
3. A. Mansourizadeh and A. F. Ismail, *J. Hazard. Mater.*, **171**, 38 (2009).
4. Z. Dai, L. Ansaloni and L. Deng, *Ind. Eng. Chem. Res.*, **55**, 5983 (2016).
5. N. A. Ahmad, C. P. Leo, A. L. Ahmad and A. W. Mohammad, *Int. J. Hydrogen Energy*, **41**, 4855 (2016).
6. A. Brunetti, F. Scura, G. Barbieri and E. Drioli, *J. Membr. Sci.*, **359**, 115 (2010).
7. S. D. Kenarsari, D. Yang, G. Jiang, S. Zhang, J. Wang, A. G. Russell, Q. Wei and M. Fan, *RSC Adv.*, **3**, 22739 (2013).
8. P. Bernardo, E. Drioli and G. Golemme, *Ind. Eng. Chem. Res.*, **48**, 4638 (2009).
9. T. L. Ward and T. Dao, *J. Membr. Sci.*, **153**, 211 (1999).
10. F. C. Gielens, R. J. J. Knibbeler, P. F. J. Duysinx, H. D. Tong, M. A. G. Vorstman and J. T. F. Keurentjes, *J. Membr. Sci.*, **279**, 176 (2006).
11. L. Liu, L. Li, Z. Ding, R. Ma and Z. Yang, *J. Membr. Sci.*, **264**, 113 (2005).
12. M. Y. Jaffrin, *J. Membr. Sci.*, **324**, 7 (2008).
13. K.-R. Hwang, C.-B. Lee, S.-K. Ryi and J.-S. Park, *Int. J. Hydrogen Energy*, **37**, 6626 (2012).
14. K.-R. Hwang, S.-W. Lee, S.-K. Ryi, D.-K. Kim, T.-H. Kim and J.-S. Park, *Fuel Process. Technol.*, **106**, 133 (2013).
15. J. Boon, J. A. Z. Pieterse, F. P. F. van Berkel, Y. C. van Delft and M. van Sint Annaland, *J. Membr. Sci.*, **496**, 344 (2015).
16. W.-H. Chen, W.-Z. Syu and C.-I. Hung, *Int. J. Hydrogen Energy*, **36**, 14734 (2011).
17. H. Takaba and S.-i. Nakao, *J. Membr. Sci.*, **249**, 83 (2005).
18. M. Grahn and J. Hedlund, *J. Membr. Sci.*, **471**, 328 (2014).
19. Á. A. Ramírez-Santos, C. Castel and E. Favre, *J. Membr. Sci.*, **526**, 191 (2017).
20. A. Shafiee, M. Arab, Z. Lai, Z. Liu and A. Abbas, *Int. J. Hydrogen Energy*, **41**, 19081 (2016).
21. V. Spallina, D. Pandolfo, A. Battistella, M. C. Romano, M. Van Sint Annaland and F. Gallucci, *Energy Convers. Manage.*, **120**, 257 (2016).
22. J. Boon, J. A. Z. Pieterse, J. W. Dijkstra, Y. C. Van Delft, P. Veenstra, Nijmeijer and D. Jansen, *Energy Procedia*, **37**, 1020 (2013).
23. F. Xie, J. Liu, J. Wang and W. Chen, *Korean J. Chem. Eng.*, **33**, 2169 (2016).
24. D. Y. Shin, K. R. Hwang, J. S. Park and M. J. Park, *Korean J. Chem. Eng.*, **32**, 1414 (2015).
25. S.-K. Ryi, J.-S. Park, K.-R. Hwang, C.-B. Lee and S.-W. Lee, *Int. J. Hydrogen Energy*, **36**, 13769 (2011).
26. J. H. Choi, M.-J. Park, J. Kim, Y. Ko, S.-H. Lee and I. Baek, *Korean J. Chem. Eng.*, **30**, 1187 (2013).
27. S. C. Brenner and L. R. Scott, *The mathematical theory of finite element methods*, 2nd Ed. Springer-Verlag, New York (2002).
28. S.-K. Ryi, J.-S. Park, K.-R. Hwang, C.-B. Lee and S.-W. Lee, *Int. J. Hydrogen Energy*, **38**, 7605 (2013).
29. F. Guazzone, E. E. Engwall and Y. H. Ma, *Catal. Today*, **118**, 24 (2006).
30. W. Liang and R. Hughes, *Chem. Eng. J.*, **112**, 81 (2005).
31. K.-R. Hwang, S.-W. Lee, D.-K. Oh, C.-B. Lee and J.-S. Park, *J. Alloys Compd.*, **685**, 337 (2016).
32. K. R. Hwang, C. B. Lee, S. K. Ryi and J. S. Park, *Int. J. Hydrogen Energy*, **37**, 6626 (2012).